



OPEN

SUBJECT AREAS:  
PHOTONIC CRYSTALS  
NANOCAVITIES  
POLARITONS  
QUANTUM OPTICS

# Photonic Architectures for Equilibrium High-Temperature Bose-Einstein Condensation in Dichalcogenide Monolayers

Jian-Hua Jiang &amp; Sajeev John

Department of Physics, University of Toronto, Toronto, Ontario, M5S 1A7 Canada.

Received  
23 September 2014Accepted  
21 November 2014Published  
11 December 2014Correspondence and  
requests for materials  
should be addressed to  
J.-H.J. (jianhua.jiang.  
phys@gmail.com)

Semiconductor-microcavity polaritons are composite quasiparticles of excitons and photons, emerging in the strong coupling regime. As quantum superpositions of matter and light, polaritons have much stronger interparticle interactions compared with photons, enabling rapid equilibration and Bose-Einstein condensation (BEC). Current realizations based on 1D photonic structures, such as Fabry-Pérot microcavities, have limited light-trapping ability resulting in picosecond polariton lifetime. We demonstrate, theoretically, above-room-temperature (up to 590 K) BEC of long-lived polaritons in MoSe<sub>2</sub> monolayers sandwiched by simple TiO<sub>2</sub> based 3D photonic band gap (PBG) materials. The 3D PBG induces very strong coupling of 40 meV (Rabi splitting of 62 meV) for as few as three dichalcogenide monolayers. Strong light-trapping in the 3D PBG enables the long-lived polariton superfluid to be robust against fabrication-induced disorder and exciton line-broadening.

Semiconductor microcavities with engineered photonic states are a valuable platform to observe fundamental and emergent quantum electrodynamic phenomena<sup>1</sup>. Polaritons are formed as a quantum superposition of semiconductor-excitons and microcavity-photons when the exciton-photon interaction is much larger than their decay rates. The ability to tailor the photonic modes, light-matter interaction and polariton lifetime in semiconductor microcavities enables versatile control of polaritons and opens the possibility of novel quantum effects such as Bose-Einstein condensation (BEC) at elevated temperatures<sup>2–6</sup>. Picosecond time-scale quasiequilibrium room-temperature polariton BEC has been claimed in ZnO<sup>7,8</sup>, GaN<sup>9–11</sup>, and polymers<sup>12</sup> in Fabry-Pérot microcavities. This is possible when the thermalization time is even shorter than the polariton lifetime. However, for both scientific studies and applications, it is more favorable to achieve room-temperature polariton BEC with polariton lifetimes on the scale of 100 ps – 1 ns. Realization of long-lived, room-temperature, equilibrium polariton BEC remains an important target for fundamental research and practical application<sup>13</sup>.

In this article, we demonstrate theoretically a route to simultaneously achieve very strong exciton-photon coupling and long polariton lifetime using a simple TiO<sub>2</sub> based photonic band gap (PBG)<sup>14,15</sup> material sandwiching a planar quantum-well slab containing as few as three monolayers of the transition-metal dichalcogenide MoSe<sub>2</sub><sup>16</sup>. This architecture provides a realistic, technologically accessible route toward equilibrium polariton BEC above room temperature. In contrast, the corresponding Fabry-Pérot microcavity has picosecond polariton lifetime due to radiative recombination into unwanted leaky (air) modes that are degenerate with the microcavity mode. These leaky modes couple strongly to any finite area polariton condensate in the quantum-well region. They are eliminated by replacing the 1D periodic structure with a 3D PBG material. Recently WSe<sub>2</sub> and MoSe<sub>2</sub> monolayers in 2D photonic crystals have been experimentally realized<sup>17,18</sup>. However, a complete 3D PBG is absent in those cavities and radiative decay of polaritons is not suppressed effectively. Another realization of a MoSe<sub>2</sub> monolayer in a Fabry-Pérot microcavity<sup>19</sup> reveals exciton-photon coupling of 31.5 meV but very rapid (sub-picosecond) polariton decay and significant line-broadening of 38.5 meV.

In a MoSe<sub>2</sub> monolayer the exciton binding energy is as large as 0.55 eV and the exciton Bohr radius is as small as 1.2 nm<sup>16,20</sup>. Theoretical calculation<sup>16</sup> predicts that 6% of incident light is absorbed during transmission through a MoSe<sub>2</sub> layer<sup>16</sup>, indicating very strong light-matter interaction. As we show, this enables high-temperature BEC with only three quantum-well monolayers of MoSe<sub>2</sub>. Previous considerations of high-temperature, equilibrium BEC have involved on the order of 100 quantum-wells<sup>21</sup>. Another special property of MoSe<sub>2</sub> is that due to



correlation between wave-vector valley and spin polarizations at the electronic band edge of MoSe<sub>2</sub>, left- and right-circularly polarized light are coupled to different exciton spin and valley states<sup>22</sup>. In other words, optical, valley, and spin polarizations are correlated with each other. Information encoded in the spin and valley channels of the condensate can be uncovered by measuring the polarization of emitted light. This may provide a new degree of freedom to store and manipulate coherent quantum information in the predicted polariton condensate<sup>23–25</sup>.

## Optical Microcavity Architectures

A fundamental challenge to the realization of above-room-temperature BEC is the accurate fabrication of complex photonic nanostructures. Almost all previous experimental studies have focused on 1D dielectric multi-layers which provide strong exciton-photon coupling at the expense of concomitant strong coupling to low-quality-factor leaky modes that render picosecond time-scale polariton lifetimes. 3D PBG materials enable very strong coupling without the occurrence of leaky modes. However, structures made of CdTe<sup>21</sup> require a very large number of embedded quantum wells in the active region to provide sufficiently strong coupling to approach room temperature BEC. Here, we propose a simple route to above-room-temperature BEC using TiO<sub>2</sub>-based photonic crystal architectures. As a reference, we provide comparison with a corresponding TiO<sub>2</sub>-SiO<sub>2</sub> 1D multi-layer photonic cavity.

In Fig. 1 we depict the Fabry-Pérot (FP), woodpile photonic crystal (PC) and slanted-pore (SP) PC microcavities, as well as their cavity-mode field intensities along the growth  $z$ -direction. There are 3 MoSe<sub>2</sub> monolayers in the middle of each microcavity separated by 7 nm TiO<sub>2</sub> layers (SiO<sub>2</sub> for the FP). Inter-layer Coulomb correlation energy is suppressed due to the large static dielectric constant ( $\sim 100$ ) of TiO<sub>2</sub> at room temperature<sup>26</sup>. The Coulomb interaction energy for two electrons (holes) separated by  $\geq 7$  nm with such high dielectric constant is  $\lesssim 2$  meV, which is much smaller than other energy scales such as the exciton-photon coupling  $\hbar\Omega = 40$  meV. Consequently, we treat excitons in each monolayer as independent. The structures of 3 microcavities are illustrated in Fig. 1a. In the woodpile PC, the height of each rod is  $h = 0.3 a$  and the width is  $w = 0.25 a$  where  $a \simeq 380$  nm is the periodicity in the  $x$ - $y$  plane (see Fig. 1a). The SP PC cavity is a SP<sub>2</sub> structure of the S/[1, 1]  $\oplus$  [-1, -1]<sup>(0.5,0)</sup> family<sup>27</sup> with the periodicity along the  $z$  direction of  $c = 1.4 a$  where  $a \simeq 370$  nm is

the in-plane lattice constant. The diameter of each cylindrical air pore is  $d = 0.69 a$ . For both types of PC microcavity, the thickness of the slab is  $0.05 a$ . The SiO<sub>2</sub>-TiO<sub>2</sub> FP cavity has two Bragg mirrors with periodicity of  $a \simeq 210$  nm and a half-wave SiO<sub>2</sub> slab of thickness  $\simeq 270$  nm in the middle, such that the lowest band edge cavity mode is close to the exciton recombination energy of 1.55 eV.

Sandwiched PC-quantum-well-PC structures<sup>28,29</sup> are fabricated in a layer-by-layer process<sup>30,31</sup>. The PCs and the quantum-well structure are fabricated independently, the quantum-well structure is then fused onto the lower PC and finally the upper PC is fused onto the quantum-well structure<sup>30,31</sup>. Corresponding technologies for TiO<sub>2</sub> PC growth have become mature in the last decade<sup>32–36</sup>. In addition, high quality MoSe<sub>2</sub> thin films can be grown by molecular beam epitaxy<sup>16</sup> and chemical vapor deposition<sup>37</sup>.

The 3D PBG's in the woodpile and the SP PC's are  $\delta\omega/\omega_c = 8.7\%$  and  $14\%$ , respectively ( $\delta\omega$  and  $\omega_c$  are the bandwidth and the central frequency of the PBG, respectively). Photonic band structures near the 3D-PBG for the woodpile and SP PC cavities reveal several confined 2D guided bands in the PBG, among which only the lowest one (depicted in Fig. 2) is relevant for polariton BEC<sup>21</sup>.

## Strong Exciton-Photon Coupling

The Hamiltonian of the coupled exciton-photon system can be written as<sup>21</sup>

$$H = \sum_{\vec{q}} \left[ \sum_{l,l_z} E_X(\vec{q}) b_{l,l_z,\vec{q}}^\dagger b_{l,l_z,\vec{q}} + \hbar\omega_{\vec{q}} a_{\vec{q}}^\dagger a_{\vec{q}} \right] + H_I, \quad (1a)$$

$$H_I = \sum_{l,l_z,\vec{q}} i\hbar\bar{\Omega}_{l,l_z,\vec{q}} \left( b_{l,l_z,\vec{q}}^\dagger a_{\vec{q}} - a_{\vec{q}}^\dagger b_{l,l_z,\vec{q}} \right), \quad (1b)$$

where  $b_{l,l_z,\vec{q}}^\dagger$  creates an exciton in the  $l$ -th monolayer with total angular momentum  $\hbar l_z = \pm \hbar$  along  $z$  direction. The energy of the  $1s$ -exciton is  $E_X(\vec{q}) = E_{X0} + \frac{\hbar^2 q^2}{2m_X}$  where  $E_{X0} = 1.55$  eV and  $m_X$  are exciton emission energy and effective mass, respectively. In this optical transition from valence to conduction band, the electron spin

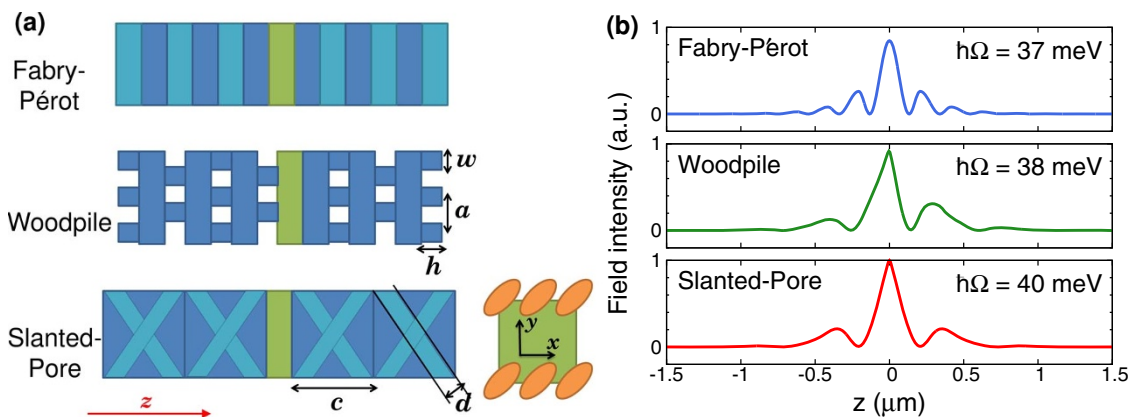


**Figure 1** | Strong coupling in microcavities (a) Schematics of the FP, woodpile PC and SP PC microcavities. Green regions in the middle represent the active layer containing 3 MoSe<sub>2</sub> monolayers embedded in TiO<sub>2</sub> for the PC cavities and SiO<sub>2</sub> for the FP cavity. For the FP cavity, the dark-blue regions are TiO<sub>2</sub> while the light-blue regions are SiO<sub>2</sub>. For woodpile PC cavity the white regions denote the air regions while the blue regions are TiO<sub>2</sub>. For SP PC cavity the light-blue regions denote slanted air pores while the dark-blue regions are TiO<sub>2</sub>. Top view of the active layer for the SP structure depicts breaking of  $x$ - $y$  symmetry due to adjacent air pores, leading to the lifting of polariton ground state degeneracy. (b) The distributions of the averaged in-plane

photonic field intensity,  $S_{u,c}^{-1} \int_{u,c} d\vec{p} \left( |\mathcal{E}_{\vec{q}}^x|^2 + |\mathcal{E}_{\vec{q}}^y|^2 \right)$  at  $\vec{Q} = (0, \frac{\pi}{a}, 0)$ , along  $z$  direction for the woodpile PC and SP PC cavities, and that at  $\vec{Q} = 0$  for the FP cavity.

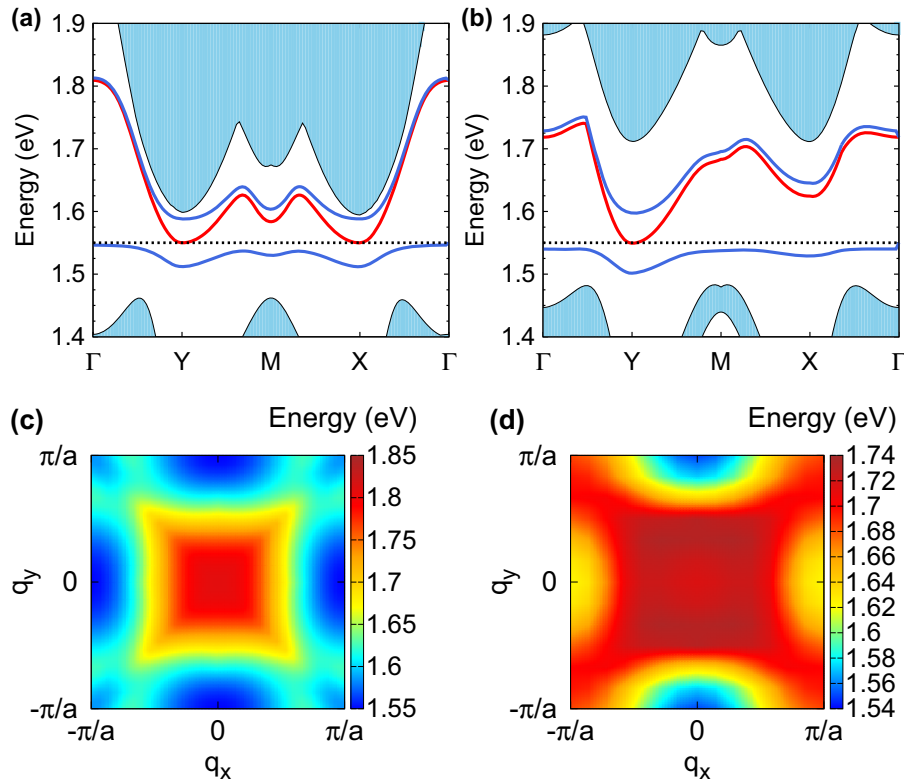


**Figure 2 | Photonic and polaritonic band structures.** Spectra of photon, exciton, and polariton for (a) woodpile and (b) SP PC microcavities. Light-blue regions are 3D photonic bands. The red curves are the lowest 2D planar guided modes, the dotted curves denote the exciton recombination energy, and the blue curves represent the upper and lower polariton branches. The lowest band edges of the 2D guided (cavity) modes are in resonance with the exciton recombination energy, 1.55 eV. This is realized when  $a = 380$  nm for the woodpile and  $a = 370$  nm for the SP PC. Spectra of the lowest 2D planar photonic band in 2D wave-vector space for woodpile (c) and SP (d) PC microcavities. The polariton ground state is doubly degenerate for the woodpile but nondegenerate for the SP microcavity.

is preserved but its orbital angular momentum changes by  $\hbar$ .  $a_{\vec{q}}^{\dagger}$  creates a photon with wave-vector  $\vec{q}$  and frequency  $\omega_{\vec{q}}$  in the lowest guided 2D photonic band. The exciton-photon coupling is

$$\hbar\bar{\Omega}_{l,I_z,\vec{q}} = \frac{d_{cv}|\phi(0)|\sqrt{\hbar\omega_{\vec{q}}}}{\sqrt{2\epsilon_0}} \sqrt{\int_{u.c.} \frac{d\vec{\rho}}{S_{u.c.}} |u_{l,\vec{q}}(\vec{\rho},z_l)|^2}, \quad (2)$$

where  $d_{cv} = 3.6 \times 10^{-29}$  Cm (Supplementary Information) is the absolute value of the interband dipole matrix element,  $\phi(0)$  is the exciton wavefunction of the 1s-excitonic state at zero electron-hole distance,  $\epsilon_0$  is the vacuum permittivity,  $S_{u.c.} = a^2$  is the area of the unit cell of PC in the  $x$ - $y$  plane,  $z_l$  is the  $z$  coordinate of the  $l$ -th MoSe<sub>2</sub> monolayer plane.  $u_{l,\vec{q}} = \vec{e}_{I_z} \cdot \vec{u}_{\vec{q}}$  where  $\vec{e}_{I_z} = \frac{1}{\sqrt{2}}(1, -iI_z, 0)$  is the polarization vector of the exciton state with  $I_z = \pm 1$  and  $\vec{u}_{\vec{q}}(\vec{r})$  is the periodic part of the photonic electric field  $\vec{E}_{\vec{q}}(\vec{r}) = \sqrt{\frac{\hbar\omega_{\vec{q}}}{2\epsilon_0 S}} \vec{u}_{\vec{q}}(\vec{r}) e^{i\vec{q}\cdot\vec{\rho}}$ . Here  $S$  is the area of the system,  $\vec{r} = (\vec{\rho}, z)$  with  $\vec{\rho} = (x, y)$  and  $S_{u.c.}^{-1} \int_{u.c.} d\vec{\rho} dz \epsilon(\vec{r}) |\vec{u}_{\vec{q}}(\vec{r})|^2 = 1$ . The special electronic band structure (see Fig. 3a) leads to optical selection rules for the lowest excitonic transitions: the  $\sigma_+$  photon excites only spin-up  $J_z = \frac{3}{2}\hbar$  hole and spin-down  $J_z = -\frac{1}{2}\hbar$  electron in the K valley, while  $\sigma_-$  photon excites only spin-down  $J_z = -\frac{3}{2}\hbar$  hole and spin-up  $J_z = \frac{1}{2}\hbar$  electron in the  $-K$  valley<sup>22,38,39</sup>. Here  $J_z$  is the total angular momentum along  $z$  direction.

The resulting dispersion of the lower polariton branch is

$$E_{lp}(\vec{q}) = \frac{E_X(\vec{q}) + \hbar\omega_{\vec{q}}}{2} - \left[ \left( \frac{E_X(\vec{q}) - \hbar\omega_{\vec{q}}}{2} \right)^2 + \hbar^2\Omega_{\vec{q}}^2 \right]^{1/2}. \quad (3)$$

Here the collective exciton-photon coupling<sup>21</sup> is given by  $\Omega_{\vec{q}}^2 = \sum_{l,I_z} |\bar{\Omega}_{l,I_z,\vec{q}}|^2$ . Strong light trapping leads to exciton-photon interaction as large as 40 meV and 38 meV in the SP PC and woodpile PC microcavities, respectively.

### Above Room Temperature Polariton BEC

The polariton BEC transition temperature,  $T_c$ , is calculated by the criterion<sup>40</sup>  $N_0/N_{tot} = 10\%$  where  $N_0$  and  $N_{tot}$  are the population on the ground state and the total polariton number respectively<sup>40</sup>. We consider a quantum box trap for polaritons with box area defined by the finite area of embedded MoSe<sub>2</sub> thin films. As shown below, the trap size, characterized by the side length  $D$  of the square box, does not alter the transition temperature considerably over a range from a few microns to one centimeter. The quantum box confinement leads to quantization of wave-vector and energy. At thermal equilibrium,  $N_0 = \left[ e^{(E_0 - \mu)/(k_B T)} - 1 \right]^{-1}$ ,  $N_{tot} = \sum_j \left[ e^{(E_j - \mu)/(k_B T)} - 1 \right]^{-1}$ , where  $E_0$  is the ground state energy,  $j$  runs over all discrete energy levels, and  $\mu$  is the chemical potential. As shown previously<sup>21</sup>,  $T_c$  is essentially defined by the polariton dispersion depth,  $V_{lp} \equiv \Delta/2 + \sqrt{(\Delta/2)^2 + \hbar^2\Omega^2}$ , where  $\Delta = E_{X0} - \hbar\omega_0$  is the exciton-photon detuning and  $\hbar\Omega \equiv \hbar\Omega_{\vec{q}(0)}$  is the exciton-photon coupling

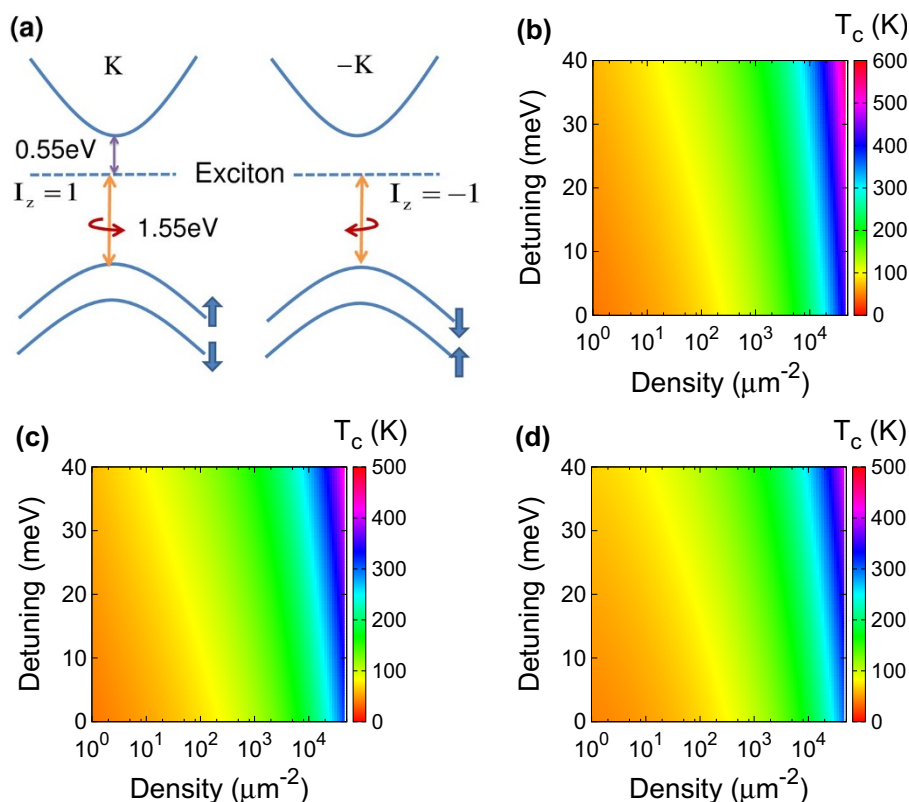


**Figure 3** | Optical selection rules and polariton BEC transition temperatures in MoSe<sub>2</sub> cavities (a) Electronic band structure and optical selection rules for MoSe<sub>2</sub>. The spin-degeneracy in the valence band is lifted by spin-orbit interaction. For an excitonic optical transition, the  $\sigma_+$  photon (angular momentum parallel to its wave-vector) is coupled to an exciton in the K valley consisting of a spin-up  $J_z = \frac{3}{2}\hbar$  hole and a spin-down  $J_z = -\frac{1}{2}\hbar$  electron. The  $\sigma_-$  photon is coupled to an exciton in the -K valley consisting of a spin-down  $J_z = -\frac{3}{2}\hbar$  hole and a spin-up  $J_z = \frac{1}{2}\hbar$  electron. Polariton BEC transition temperature  $T_c$  vs. detuning  $\Delta$  and polariton density for (b) SP PC, (c) woodpile PC and (d) FP microcavities. The side length of the square-shaped exciton-trap is  $D = 5 \mu\text{m}$ .

at photonic band edge. As  $k_B T$  approaches  $V_{lp}$ , the population on exciton-like states with very large effective mass becomes significant<sup>21</sup>. The pure exciton BEC transition temperature is calculated to be less than 4 K for density less than  $(10a_B)^{-2}$  and trap size  $D$  of 1 micron in a MoSe<sub>2</sub> monolayer. On the other hand for positive detuning  $\Delta = 30$  meV and  $\hbar\Omega = 40$  meV, the dispersion depth is 58 meV. This can support polariton BEC up to  $V_{lp}/k_B \approx 600$  K.

Figs. 3(b)–(d) give the polariton BEC transition temperatures for different detuning  $\Delta$  and polariton densities for the SP PC, woodpile PC, and FP cavities. We assume that the exciton gas is initially created by incoherent pumping that (after thermal relaxation) equally populates all degenerate dispersion minima ( $\vec{Q}$ -points) in the photonic band structure. As seen in Fig. 2, the woodpile PC has a doubly degenerate polariton minimum whereas the polariton ground state is nondegenerate for the SP PC. The trap size is  $D = 5 \mu\text{m}$ . The  $T_c$  is enhanced with increasing detuning as the polariton dispersion depth increases. The highest  $T_c$  is reached at the largest detuning  $\Delta = 40$  meV which is 590 K, 450 K, and 430 K for the SP PC, woodpile PC and FP cavities, respectively. The BEC transition temperature  $T_c$  is highest in the SP PC cavity since it contains a nondegenerate polariton ground state. This is provided by the placement of the active layer at a plane that breaks the  $x$ - $y$  symmetry of the criss-crossing pores above and below (see Fig. 1a). In contrast, there are two degenerate polariton minima in the woodpile that reduces effective polariton density for BEC by a factor of two. In the case of the FP cavity, the polariton density available for BEC is divided by the two degenerate optical polarization states at  $\vec{Q} = 0$ . We do not

consider larger detuning because a too large  $\Delta$  will reduce the exciton fraction of polariton as well as the polariton-phonon and polariton-polariton scattering, which leads to much longer equilibration time.

The polariton BEC transition temperatures at  $\Delta = 30$  meV for different trap sizes  $D$  and polariton densities for each cavity are shown in Fig. 4. The trap size dependence is prominent for low polariton densities, but very weak for high polariton densities<sup>21</sup>. At low densities,  $k_B T_c \ll V_{lp}$  and polariton equilibrium is governed by the low-lying excited states of very small effective mass particles in the box trap that are very sensitive to  $D$ . At high polariton densities,  $k_B T_c \lesssim V_{lp}$  and a significant fraction of polaritons acquire the bare exciton mass for which the level spacing is less sensitive to  $D$ . Eventually  $T_c$  tends to zero for very large trap size  $D$  (when the low-lying excited states are extremely close to the ground state) according to the Mermin-Wagner theorem<sup>41</sup>. In all these calculations the largest polariton density,  $5 \times 10^4 \mu\text{m}^{-2}$ , corresponds to an exciton density in each MoSe<sub>2</sub> monolayer less than  $(11a_B)^{-2}$ , well below the exciton saturation density of  $(5a_B)^{-2}$ <sup>42</sup>.

Fabrication induced disorder and exciton line broadening tend to degrade high-temperature polariton BEC. In a PBG material, light in the cavity mode is well-protected from scattering into unwanted modes. Consequently, the role of disorder is primarily to shift the cavity resonance frequency. For photonic (dielectric) disorder, our calculation indicates that in the woodpile and SP PC cavities, photonic structure deviations less than 6 nm in the active slab layer, less than 12 nm in the logs close to the active slab layer, or less than 20 nm in the logs two periods away, do not affect the band edge of



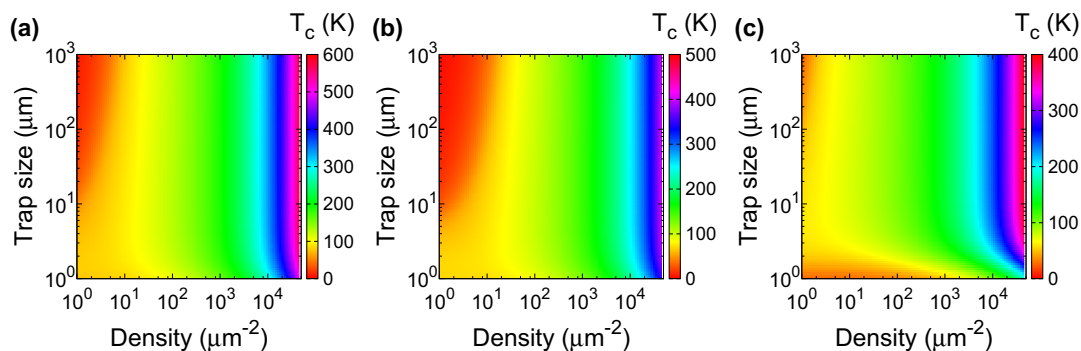


**Figure 4 | High-temperature polariton BEC** Polariton BEC transition temperature  $T_c$  vs. trap size and polariton density for (a) SP PC, (b) woodpile PC, (c) FP microcavities. Detuning is  $\Delta = 40$  meV, corresponding to  $\lambda = 820$  nm for the FP cavity,  $a = 390$  nm for woodpile PC cavity, and  $a = 380$  nm for SP PC cavity.

the lowest planar guided mode by more than 2%. This fluctuation is equivalent to alteration of the detuning by  $\pm 30$  meV, which can reduce the  $T_c$  to 360 K (480 K) if the detuning decreases to 10 meV for the woodpile (SP) PC cavity. Polariton BEC is also found to be robust to exciton homogeneous and inhomogeneous broadening although the Rabi-splitting and polariton dispersion depth are slightly reduced (e.g., Rabi splitting in SP cavity is reduced from 80 meV to 62 meV) (see Supplementary Information).

In contrast there is no 3D PBG for the FP cavity and light-trapping is not robust to disorder. Excitons in the FP with wave-vector  $q \gtrsim 0.3q_0$  with  $q_0 = E_{X0}/(\hbar c)$  are strongly coupled to leaky (air) modes, leading to rapid radiative decay<sup>43</sup>. This decay into leaky modes is not alleviated by increasing the quality of the FP cavity mode and is exacerbated by imperfect fabrication accuracy. In real FP cavities, dielectric disorder scatters polaritons with wave-vector  $q \sim 0$  into leaky modes with the same energy. Such scattering significantly limits the quality factor of the (nonleaky) cavity mode ( $\sim 10^3$ ). The overall polariton lifetime due to radiative decay is very short ( $\lesssim 1$  ps) in  $\text{SiO}_2/\text{TiO}_2$  multilayers<sup>44</sup> and in other<sup>8</sup> FP cavities. The resulting sub-picosecond polariton lifetime (see also calculation in the Supplementary Information) is still comparable with the thermalization time, although calculations have shown that phonon scattering is very efficient (about 0.1 ps scattering time) in  $\text{MoSe}_2$  at room temperature<sup>45</sup>. In contrast, PC cavities protected by a 3D PBG enable light-trapping in all directions, leading to polaritons with lifetime limited only by nonradiative decay (see Supplementary Information). This nonradiative decay is further suppressed by our detuning ( $\Delta > 0$ ) that renders our polariton more photon-like than exciton-like. The quantum coherence of polaritons in the cavity can be probed and manipulated using light propagating through engineered waveguide channels in the 3D PBG cladding<sup>31,46</sup>.

In the absence of any microcavity, optically excited valley polarization of excitons can last only about 9 ps in  $\text{MoSe}_2$  at room temperature<sup>47</sup>. In high-quality PC microcavities strong light trapping over all directions can enhance polariton lifetime beyond 130 ps (the exciton lifetime in  $\text{MoSe}_2$  monolayer without any cavity at room temperature)<sup>47</sup>. When the polaritons form a BEC, optical, valley, and spin polarization coherences maintained on such long time-scales may be useful for quantum information processing based on manipulation of the spin and valley degrees of freedom<sup>24,25</sup>.

## Conclusions

We have theoretically demonstrated photonic crystal architectures based on  $\text{TiO}_2$  with very strong light-matter interaction and long polariton lifetime for above-room-temperature, equilibrium exciton-polariton BEC. The 3D photonic band gap robustly supports strongly confined guided modes in a slab cavity containing three separated excitonic  $\text{MoSe}_2$  monolayers. Unlike 1D periodic Fabry-Pérot structures that suffer from substantial radiative decay through directions

other than the stacking direction, the 3D PBG structures suppress radiative decay in all directions enabling equilibration and long-time polariton coherence. An important feature of the slanted pore PC architecture is that it provides a non-degenerate lower polariton dispersion minimum, without recourse to a symmetry-breaking external field<sup>23</sup>. This enables a remarkable equilibrium high-temperature Bose-Einstein condensate, above 500 K, with only three quantum well layers. Both  $\text{TiO}_2$  based photonic crystals and  $\text{MoSe}_2$  thin films have been fabricated with mature technologies providing a very accessible route to high-temperature BEC. This BEC is robust to disorder, fabrication imperfections, exciton homogeneous and inhomogeneous line-broadening. The unique coupling among the optical, valley, and spin degrees of freedom in  $\text{MoSe}_2$  provides a condensate with novel internal symmetries that can be manipulated by external fields. Polariton BEC with long-lived optical, valley, and spin coherence persisting above room-temperature offers new opportunities for macroscopic quantum physics.

## Methods

The photonic band structures and electric field distributions for PC microcavities are calculated using the plane wave expansion method, while those for the FP microcavity are calculated using the transfer matrix method. The refractive indices of  $\text{TiO}_2$  and  $\text{SiO}_2$  are 2.7 and 1.5, respectively<sup>48</sup>. In  $\text{MoSe}_2$  the effective mass for conduction band electron and valence band hole are,  $m_e = 0.7 m_0$  and  $m_h = 0.55 m_0$ , respectively<sup>49</sup>. The effective mass of exciton is  $m_X = m_e + m_h$ . The exciton Bohr radius  $a_B$  and interband band dipole matrix element  $d_{cv}$  are obtained from existing studies on electronic band structure in  $\text{MoSe}_2$  and excitonic optical absorption<sup>16,22</sup> (see Supplementary Information). The calculation of  $T_c$  involves summation over numerous polariton states which is broken into two parts: the summation over the first 1600 states and the integration over other higher states. Polariton energy in a square (hard-wall) quantum box is calculated according to wave-vector quantization.

1. Yamamoto, Y., Tassone, T. & Cao, H. *Semiconductor cavity quantum electrodynamics*. (Springer, Berlin, 2000).
2. Deng, H., Weihs, G., Santori, C., Bloch, J. & Yamamoto, Y. Condensation of semiconductor microcavity exciton polaritons. *Science* **298**, 199–202 (2002).
3. Kasprzak, J. *et al.* Bose-Einstein condensation of exciton polaritons. *Nature* **443**, 409–414 (2006).
4. Balili, R., Hartwell, V., Snoke, D., Pfeiffer, L. & West, K. Bose-Einstein condensation of microcavity polaritons in a trap. *Science* **316**, 1007–1010 (2007).
5. Kasprzak, J., Solnyshkov, D. D., André, R., Dang, L. S. & Malpuech, G. Formation of an exciton polariton condensate: thermodynamic versus kinetic regimes. *Phys. Rev. Lett.* **101**, 146404 (2008).
6. Deng, H., Haug, H. & Yamamoto, Y. Exciton-polariton Bose-Einstein condensation. *Rev. Mod. Phys.* **82**, 1489–1537 (2010).
7. Lai, Y.-Y., Lan, Y.-P. & Lu, T.-C. Strong light-matter interaction in ZnO microcavities. *Light Sci. Appl.* **2**, e76 (2013).
8. Li, F. *et al.* From excitonic to photonic polariton condensate in a ZnO-based microcavity. *Phys. Rev. Lett.* **110**, 196406 (2013).
9. Christopoulos, S. *et al.* Room-temperature polariton lasing in semiconductor microcavities. *Phys. Rev. Lett.* **98**, 126405 (2007).
10. Christmann, G., Butté, R., Feltn, E., Carlin, J.-F. & Grandjean, N. Room temperature polariton lasing in a GaN/AlGaIn multiple quantum well microcavity. *Appl. Phys. Lett.* **93**, 051102 (2008).



11. Levrat, J. *et al.* Condensation phase diagram of cavity polaritons in GaN-based microcavities: experiment and theory. *Phys. Rev. B* **81**, 125305 (2010).
12. Plumhof, J. D., Stöferle, T., Mai, L., Scherf, U. & Mahrt, R. F. Room-temperature Bose-Einstein condensation of cavity exciton-polaritons in a polymer. *Nat. Mater.* **13**, 247–252 (2014).
13. Snoke, D. Microcavity polaritons: a new type of light switch. *Nat. Nanotechnol.* **8**, 393–395 (2013).
14. John, S. Strong localization of photons in certain disordered dielectric superlattices. *Phys. Rev. Lett.* **58**, 2486–2489 (1987).
15. Yablonoitch, E. Inhibited spontaneous emission in solid-state physics and electronics. *Phys. Rev. Lett.* **58**, 2059–2062 (1987).
16. Ugeda, M. M. *et al.* Observation of giant bandgap renormalization and excitonic effects in a monolayer transition metal dichalcogenide semiconductor. arXiv:1404.2331, *Nat. Mater.* in press.
17. Gan, X. *et al.* Controlling the spontaneous emission rate of monolayer MoS<sub>2</sub> in a photonic crystal nanocavity. *Appl. Phys. Lett.* **103**, 181119 (2013).
18. Wu, S. *et al.* Control of two-dimensional excitonic light emission via photonic crystal. *2D Mater.* **1**, 011001 (2014).
19. Liu, X. *et al.* Strong light-matter coupling in two-dimensional atomic crystals. arXiv: 1406.4826.
20. Ross, J. S. *et al.* Electrical control of neutral and charged excitons in a monolayer semiconductor. *Nat. Commun.* **4**, 1474 (2013).
21. Jiang, J. H. & John, S. Photonic crystal architecture for room temperature equilibrium Bose-Einstein condensation of exciton-polaritons. *Phys. Rev. X* **4**, 031025 (2014).
22. Xiao, D., Liu, G.-B., Feng, W., Xu, X. & Yao, W. Coupled spin and valley physics in monolayers of MoS<sub>2</sub> and other group-VI dichalcogenides. *Phys. Rev. Lett.* **108**, 196802 (2012).
23. Schneider, C. *et al.* An electrically pumped polariton laser. *Nature* **497**, 348–352 (2013).
24. Amo, A. *et al.* Exciton-polariton spin switches. *Nature Photon.* **4**, 361–366 (2010).
25. Cerna, R. *et al.* Ultrafast tristable spin memory of a coherent polariton gas. *Nat. Commun.* **4**, 2008 (2013).
26. Parker, R. A. Static dielectric constant of rutile (TiO<sub>2</sub>), 1.6–1060 K. *Phys. Rev.* **124**, 1719–1722 (1961).
27. Toader, O., Berciu, M. & John, S. Photonic band gaps based on tetragonal lattices of slanted pores. *Phys. Rev. Lett.* **90**, 233901 (2003).
28. John, S. & Yang, S. Electromagnetically induced exciton mobility in a photonic band gap. *Phys. Rev. Lett.* **99**, 046801 (2007).
29. Yang, S. & John, S. Exciton dressing and capture by a photonic band edge. *Phys. Rev. B* **75**, 235332 (2007).
30. Ogawa, S., Imada, M., Yoshimoto, S., Okano, M. & Noda, S. Control of light emission by 3D photonic crystals. *Science* **305**, 227–229 (2004).
31. Noda, S., Fujita, M. & Asano, T. Spontaneous-emission control by photonic crystals and nanocavities. *Nature Photon.* **1**, 449–458 (2007).
32. Noda, S., Tomoda, K., Yamamoto, N. & Chutinan, A. Full three-dimensional photonic bandgap crystals at near-infrared wavelengths. *Science* **289**, 604–606 (2000).
33. Nelson, E. *et al.* Epitaxial growth of three-dimensionally architecture optoelectronic devices. *Nat. Mater.* **10**, 676–681 (2011).
34. King, J. S. *et al.* Infiltration and inversion of holographically defined polymer photonic crystal templates by atomic layer deposition. *Adv. Mater.* **18**, 1561–1565 (2006).
35. Deubel, M., Wegener, M., Kaso, A. & John, S. Direct laser writing and characterization of “slanted-pore” photonic crystals. *Appl. Phys. Lett.* **85**, 1895–1897 (2004).
36. Deubel, M. *et al.* Direct laser writing of three-dimensional photonic-crystal templates for telecommunications. *Nat. Mater.* **3**, 444–447 (2004).
37. Shim, G. W. *et al.* Large-area single-layer MoSe<sub>2</sub> and its van der Waals heterostructures. *ACS Nano* **8**, 6655–6662 (2014).
38. Zeng, H., Dai, J., Yao, W., Xiao, D. & Cui, X. Valley polarization in MoS<sub>2</sub> monolayers by optical pumping. *Nat. Nanotechnol.* **7**, 490–493 (2012).
39. Mak, K. F., He, K., Shan, J. & Heinz, T. F. Control of valley polarization in monolayer MoS<sub>2</sub> by optical helicity. *Nat. Nanotechnol.* **7**, 494–498 (2012).
40. Penrose, O. & Onsager, L. Bose-Einstein condensation and liquid helium. *Phys. Rev.* **104**, 576–584 (1956).
41. Mermin, N. D. & Wagner, H. Absence of Ferromagnetism or antiferromagnetism in one- or two-Dimensional isotropic Heisenberg models. *Phys. Rev. Lett.* **17**, 1133–1136 (1966).
42. Schmitt-Rink, S., Chemla, D. S. & Miller, D. A. B. Theory of transient excitonic optical nonlinearities in semiconductor quantum-well structures. *Phys. Rev. B* **32**, 6601–6609 (1985).
43. Savona, V. & Tassone, F. Exact Quantum Calculation of polariton dispersion in semiconductor microcavities. *Solid State Commun.* **95**, 673–678 (1995).
44. Bhattacharya, P. *et al.* Room temperature electrically injected polariton laser. *Phys. Rev. Lett.* **112**, 236802 (2014).
45. Jin, Z., Li, X., Mullen, J. T. & Kim, K. W. Intrinsic transport properties of electrons and holes in monolayer transition-metal dichalcogenides. *Phys. Rev. B* **90**, 045422 (2014).
46. Chutinan, A., John, S. & Toader, O. Diffractionless flow of light in all-optical microchips. *Phys. Rev. Lett.* **90**, 123901 (2003).
47. Kumar, N., He, J., He, D., Wang, Y. & Zhao, H. Valley and spin dynamics in MoSe<sub>2</sub> two-dimensional crystals. *Nanoscale*, **6**, 12690 (2014).
48. Landmann, M., Rauls, E. & Schmidt, W. G. The Electronic structure and optical response of rutile, anatase and brookite TiO<sub>2</sub>. *J. Phys.: Condens. Matter* **24**, 195503 (2012).
49. Ramasubramaniam, A. Large excitonic effects in monolayers of molybdenum and tungsten dichalcogenides. *Phys. Rev. B* **86**, 115409 (2012).

## Acknowledgments

We thank J. E. Sipe, J.-L. Cheng, and R. A. Muniz for helpful discussions. This work was supported by the Natural Sciences and Engineering Research Council of Canada and the United States Department of Energy through Contract No. DE-FG02-06ER46347.

## Author contributions

J.-H.J. performed calculations and analysis. S.J. guided the research.

## Additional information

**Supplementary information** accompanies this paper at <http://www.nature.com/scientificreports>

**Competing financial interests:** The authors declare no competing financial interests.

**How to cite this article:** Jiang, J.-H. & John, S. Photonic Architectures for Equilibrium High-Temperature Bose-Einstein Condensation in Dichalcogenide Monolayers. *Sci. Rep.* **4**, 7432; DOI:10.1038/srep07432 (2014).



This work is licensed under a Creative Commons Attribution-NonCommercial-NoDerivs 4.0 International License. The images or other third party material in this article are included in the article's Creative Commons license, unless indicated otherwise in the credit line; if the material is not included under the Creative Commons license, users will need to obtain permission from the license holder in order to reproduce the material. To view a copy of this license, visit <http://creativecommons.org/licenses/by-nc-nd/4.0/>